

Shape Estimation and Tracking using Spherical Double Fourier Series for Three-Dimensional Range Sensors

Tim Baur¹, Johannes Reuter¹, Antonio Zea² and Uwe D. Hanebeck²

Abstract—In this paper, a novel measurement model based on spherical double Fourier series (DFS) for estimating the 3D shape of a target concurrently with its kinematic state is introduced. Here, the shape is represented as a star-convex radial function, decomposed as spherical DFS. In comparison to ordinary DFS, spherical DFS do not suffer from ambiguities at the poles. Details will be given in the paper. The shape representation is integrated into a Bayesian state estimator framework via a measurement equation. As range sensors only generate measurements from the target side facing the sensor, the shape representation is modified to enable application of shape symmetries during the estimation process. The model is analyzed in simulations and compared to a shape estimation procedure using spherical harmonics. Finally, shape estimation using spherical and ordinary DFS is compared to analyze the effect of the pole problem in extended object tracking (EOT) scenarios.

I. INTRODUCTION

As the resolution and accuracy of modern sensors increases, more information can be extracted out of recorded environment data when applying appropriate measurement models. When multiple measurements per time step from a single target are gathered, estimating the targets extent during the tracking procedure [1] instead of tracking the target as a single point is feasible. This procedure is known as EOT. Nowadays, tracking extended objects has to be performed in a variety of disciplines including robotics and autonomous systems and in different environments like on-road, off-road or in maritime systems.

In EOT, different approaches to model the target extent and shape have been proposed. Early approaches model the shape using a spatial distribution [2] that associates the shape parameters with the observed measurements. A famous and frequently used example are the well-known random matrices [3]. However, spatial distribution models are complicated to derive and not very flexible in terms of different shapes or even shape estimation techniques. In contrast, random hypersurface models [4] try to associate a measurement to a specific measurement source by application of a greedy association rule. Thus, measurements can easily be associated to measurement sources gathered from various shapes and even shape estimation techniques can be developed. However, one

major drawback of these models is that by adopting a greedy association rule, an estimation bias is introduced [5], [6].

If prior knowledge of the target extent is available, basic geometric shapes such as rectangles [7], [8], [9] or ellipses [3], [4] can be applied in EOT. For example, ellipses approximate the top view shape of a ship reasonably well and can be applied in maritime environments. In contrast, rectangles in 2D or cuboids in 3D space nearly perfectly fit targets like cars and are applied in automotive applications. However, in many cases prior knowledge is not available or many targets with different shapes are present. A solution to this problem is to estimate the shape itself [10], [11] during the tracking procedure, avoiding to potentially corrupt the estimation outcome by modeling the measurement sources on the target accurately.

If 3D contour measurements gathered by devices such as multilayer LiDAR sensors or depth cameras are available, shape estimation algorithms using Gaussian processes [12], [13], [14] or spherical harmonics [15] for star-convex shape representation can be applied. In addition, 3D EOT measurement models using basic geometric shapes [16], [17] or restricted shape estimation [18] have been proposed if prior knowledge is available, detailed shape information is not required in the application or computational complexity is to be reduced.

The contribution of this paper is to propose a novel measurement model that allows for concurrent shape and pose estimation of an extended object in 3D space using spherical DFS [19]. Using ordinary DFS, functions defined on a rectangular domain $[x, y] \in [a, b] \times [c, d]$ can be decomposed. However, when radial functions are defined on the unit sphere $[\theta, \phi] \in [0, \pi] \times [0, 2\pi]$, the rectangular domain is mapped to the surface of a sphere that differs completely from a rectangle. Thus, ambiguities at the poles where the domain resolves into a single point are imposed on the radial function, see Fig. 1. Spherical DFS can handle this issue in analogy to spherical harmonics but have some nice advantages for EOT in comparison. In order to estimate the 3D shape concurrently to the target pose, we propose a greedy association model using a proper association rule. The model can be applied to 3D contour measurements. In order to enable modeling the possibly unseen backside of the target, we propose a second representation of spherical DFS where the radial function is “even” in azimuth angle ϕ introducing a vertical plane of symmetry.

An advantage of 3D shape estimation is the possibility of target classification using 3D range sensors. In contrast to visual sensors, depth devices such as multilayer LiDAR

¹T. Baur and J. Reuter are with the Institute of System Dynamics (ISD), University of Applied Sciences Konstanz (HTWG), Germany, Email: tbaur@htwg-konstanz.de, jreuter@htwg-konstanz.de

²A. Zea and U. D. Hanebeck are with the Intelligent Sensor-Actuator-Systems Laboratory (ISAS), Institute for Anthropomatics and Robotics, Karlsruhe Institute of Technology (KIT), Germany, Email: antonio.zea@kit.edu, uwe.hanebeck@kit.edu

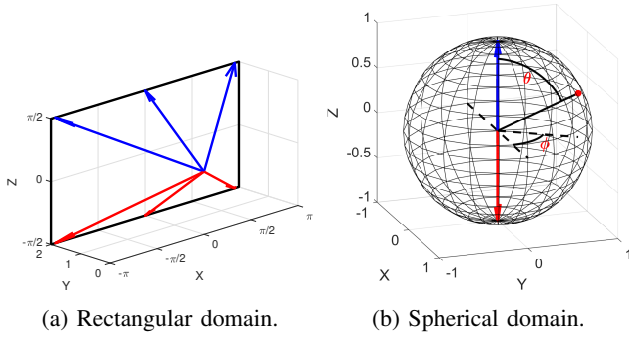


Fig. 1: Illustration of pole problem and different domains.

sensors can still be used without ambient light justifying classification with these sensors. It is indisputable that classification must be an essential part in many automated and autonomous systems for scene interpretation and prediction.

The remainder of this paper is organized as follows. Our model is based on work done over the past fifty years by the international meteorological society in order to model and predict atmospheric circulations and physics. Sec. II is therefore devoted to spherical DFS, its properties, and the redefinition of spherical DFS to incorporate a vertical plane of symmetry. These representations of a star-convex radial function are then included in a greedy association measurement model in Sec. III to be able to concurrently estimate the targets shape and pose. Subsequently, our model is investigated and compared to a model using spherical harmonics [15] in simulated scenarios in Sec. IV. For a better understanding of the pole problem in EOT, spherical and ordinary DFS measurement models are compared in Sec. V. Finally, the paper ends with conclusions and future work in Sec. VI.

II. SPHERICAL DOUBLE FOURIER SERIES

Representing arbitrary star-convex shapes can be achieved by using radial functions $r(\theta, \phi)$ as contour functions where angle pairs $(\theta, \phi)^T$ are mapped to the radius r of the contour, see Fig. 1b. As stated before, ordinary truncated DFS of the form

$$r(\theta, \phi) = \sum_{m=-N}^N \sum_{l=-N}^N c_{m,l} \exp(2il\theta) \exp(im\phi) \quad (1)$$

representing star-convex radial functions are defined on the rectangular domain $[\theta, \phi] \in [0, \pi) \times [0, 2\pi)$, see Fig. 1a. However, a spherical domain differs completely from a rectangular one, see Fig. 1b. Thus, using (1) for representation of star-convex radial functions suffers from ambiguities at the poles $\theta = 0$ and $\theta = \pi$ as the surface of a sphere cannot be unwrapped into a rectangle. In Fig. 1 this is illustrated with blue and red arrows for north and south poles, respectively. As can be seen, for a rectangular domain in Fig. 1a different north and south poles can be found in comparison to a spherical domain in Fig. 1b. For more details on the pole problem the reader is referred to [20].

A. Spherical cosine-sine DFS

In order to decompose a radial function to angles θ and ϕ , the representation has to meet several boundary conditions to ensure continuity at the poles [20]. Using spherical harmonics, these boundary conditions are naturally met. However, when using DFS some considerations must be made. First, the radial function is expanded to a truncated Fourier series for angle ϕ as

$$r(\theta, \phi) = \sum_{m=-N}^N r_m(\theta) \exp(im\phi) \quad (2)$$

where $r_m(\theta)$ is the decomposition in angle θ . A first suggestion for spherical DFS was presented in [21]. However, constraints were necessary as discontinuities at the poles were still present without. Several other representations were compared in [22]. Note that spherical harmonics and spherical DFS representation only differ in the decomposition of $r_m(\theta)$ where spherical harmonics use associated Legendre polynomials, while spherical DFS use a Fourier series decomposition. A comparison of both approaches is given in [20], [23]. In this paper we use the decomposition proposed by Cheong [19], [24] given as

$$r_m(\theta) = \begin{cases} \sum_{l=0}^N \psi_{m,l} \cos(l\theta) & \text{for } m = 0 \\ \sum_{l=1}^N \psi_{m,l} \sin(l\theta) & \text{for odd } m \\ \sum_{l=1}^N \psi_{m,l} \sin(\theta) \sin(l\theta) & \text{for even } m \neq 0 \end{cases} \quad (3)$$

where $\psi_{m,l}$ are the complex Fourier coefficients. In order for the spherical DFS to be applicable in a nonlinear Gaussian state estimator we propose to use the cosine-sine representation given as

$$r(\theta, \phi) = a_0(\theta) + \sum_{m=1}^N \sum_{l=1}^N a_{m,l} \sin^s(\theta) \sin(l\theta) \cos(m\phi) + \sum_{m=1}^N \sum_{l=1}^N b_{m,l} \sin^s(\theta) \sin(l\theta) \sin(m\phi) \quad (4)$$

with

$$a_0(\theta) = \sum_{l=0}^N a_{0,l} \cos(l\theta) \quad (5)$$

and

$$s = \begin{cases} 0 & \text{for odd } m \\ 1 & \text{for even } m \end{cases} \quad (6)$$

B. Vertical plane of symmetry

As already stated above, devices such as multilayer LiDAR sensors or depth cameras gather 3D range data from the targets side facing the sensor. Thus, modeling the backside of the target is essential in shape estimation. This can be achieved by involving a vertical plane of symmetry in the shape estimation procedure. Such an assumption is reasonable as many real world targets such as cars or ships in maritime environments involve a vertical plane of symmetry along their length axis. When using spherical DFS, a vertical plane of symmetry can be integrated by forcing the function to be even in the azimuth angle ϕ . This can be achieved by discarding the sine components of the Fourier series

belonging to the azimuth angle ϕ [25], [26]. The spherical DFS is then given as

$$r(\theta, \phi) = a_0(\theta) + \sum_{m=1}^N \sum_{l=1}^N a_{m,l} \sin^s(\theta) \sin(l\theta) \cos(m\phi) \quad (7)$$

where $a_0(\theta)$ and s are still given by (5) and (6), respectively.

III. MEASUREMENT MODEL

In the following, the measurement model to enable concurrent shape estimation and tracking is presented. Therefore, the hidden system state is given as

$$\underline{x}_k = \left[\underline{m}_k^T, \underline{\varphi}_k^T, \underline{\dot{x}}_k^T, \underline{p}_k^T \right]^T \quad (8)$$

with center \underline{m}_k , orientation vector $\underline{\varphi}_k$, velocity components $\underline{\dot{x}}_k$, and shape parameters \underline{p}_k . Note that the orientation vector $\underline{\varphi}_k$ possibly contains all three rotation angles yaw, pitch, and roll in 3D space. According to [13], also quaternions can be used as rotational representation in order to prevent gimbal locks in 3D space but this goes beyond the scope of this paper. According to Sec. II, the shape parameters are given as

$$\underline{p}_k = [a_{00}, a_{10}, \dots, a_{11}, a_{12}, \dots, b_{11}, b_{12}, \dots]^T \in \mathbb{R}^{d_p} \quad (9)$$

for a full spherical DFS with $d_p = N + 1 + 2N^2$ coefficients or as

$$\underline{p}_k = [a_{00}, a_{10}, \dots, a_{11}, a_{12}, \dots]^T \in \mathbb{R}^{d_p} \quad (10)$$

for spherical DFS with a vertical plane of symmetry with $d_p = N + 1 + N^2$ coefficients. As comparison, for a measurement model using spherical harmonics [15] $d_p = 4N^2 + 4N + 1$ coefficients are needed for both a full decomposition and for a decomposition involving a vertical plane of symmetry. The hidden system state is about to be estimated in a nonlinear state estimator using the measurement set $\mathbf{Z}_k = \left\{ z_{k,l} \right\}_{l=1}^{m_k}$ gathered at time step k . The objective of the measurement equation is to link the measurement set with the hidden system state. In this case the measurements are assumed to be gathered based on a measurement source model

$$z_{k,l} = \underline{y}_{k,l} + \underline{v}_{k,l} \quad (11)$$

with measurement source $\underline{y}_{k,l}$ and white Gaussian zero-mean noise term $\underline{v}_{k,l} \sim \mathcal{N}(0, \Sigma_v)$. Due to the assumption of gathered contour measurements, the measurement sources are located on the target boundary $\mathcal{B}(\underline{p}_k)$ given as

$$\underline{y}_{k,l} \in \underline{m}_k + \mathcal{B}(\underline{p}_k) \quad (12)$$

Substituting (12) into (11), the measurement can be related to the targets boundary given as

$$z_{k,l} \in \underline{m}_k + \mathcal{B}(\underline{p}_k) + \underline{v}_{k,l} \quad (13)$$

Using (13), various measurement models can be derived by plugging in a desired parametric shape representation for $\mathcal{B}(\underline{p}_k)$. In this paper we are aiming to estimate the targets outer contour by representing the shape using spherical DFS

$$r_{k,l} = r(\theta_{k,l}, \phi_{k,l}) \quad (14)$$

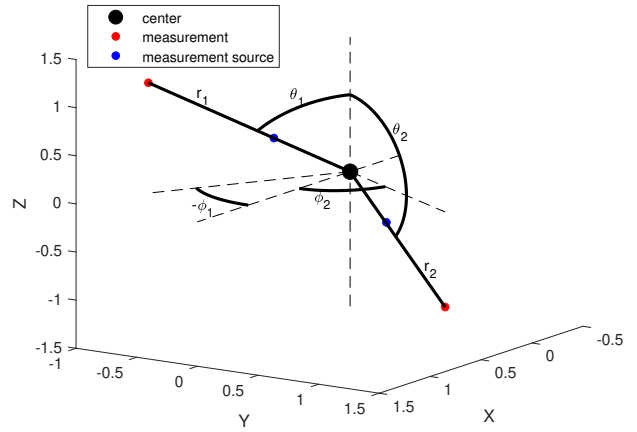


Fig. 2: Illustration of measurement source association rule.

of (4) or (7) presented in Sec. II. Given a proper shape representation, the final measurement equation can be represented as

$$z_{k,l} = \underline{m}_k + \underline{q}(\underline{m}_k) r(\hat{\theta}_{k,l}, \hat{\phi}_{k,l}) + \underline{v}_{k,l} \quad (15)$$

with unit length orientation vector $\underline{q}(\underline{m}_k) = \frac{z_{k,l} - \underline{m}_k}{\|z_{k,l} - \underline{m}_k\|}$ and measurement source $(\hat{\theta}_{k,l}, \hat{\phi}_{k,l})$. As the measurement source on the targets outer contour is unknown we adopt a greedy measurement source association rule. The association rule we use in this publication is illustrated in Fig. 2. The measurement source is assumed to be located at the intersection of a straight line from center to measurement with the predicted shape. This association rule is very comfortable as the measurement source is calculated quite easily. However, also different association rules such as taking the closest point on the contour to the measurement can be applied. Here, the measurement in local coordinates given as

$$\hat{z}_{k,l} = \mathbf{R}_{\varphi_k}^{-1} (z_{k,l} - \underline{m}_k) \quad (16)$$

with rotation matrix \mathbf{R}_{φ_k} is needed for calculating the measurement source. Note that the rotation matrix is not limited to a single rotation but rather can be applied to all three spatial axes. Then the measurement source can be calculated as

$$\hat{\theta}_{k,l} = \arccos \left(\frac{x_{\hat{z}_{k,l}}}{\|\hat{z}_{k,l}\|} \right), \quad (17)$$

$$\hat{\phi}_{k,l} = \text{atan2}(y_{\hat{z}_{k,l}}, x_{\hat{z}_{k,l}}) \quad (18)$$

with $x_{\hat{z}_{k,l}}$ and $y_{\hat{z}_{k,l}}$ as x and y coordinate of $\hat{z}_{k,l}$, respectively. Using (15), our shape estimation algorithm is implemented with an unscented Kalman filter [27] in this paper. However, any other nonlinear state estimation technique can be applied.

IV. SIMULATION EXPERIMENTS

In this section, our shape estimation algorithm is investigated in simulated static and dynamic scenarios. In the static scenario, only the Fourier coefficients defining the shape are estimated and compared to the procedure using spherical harmonics [15]. Afterwards, our shape estimation procedure is investigated in a dynamic tracking scenario.

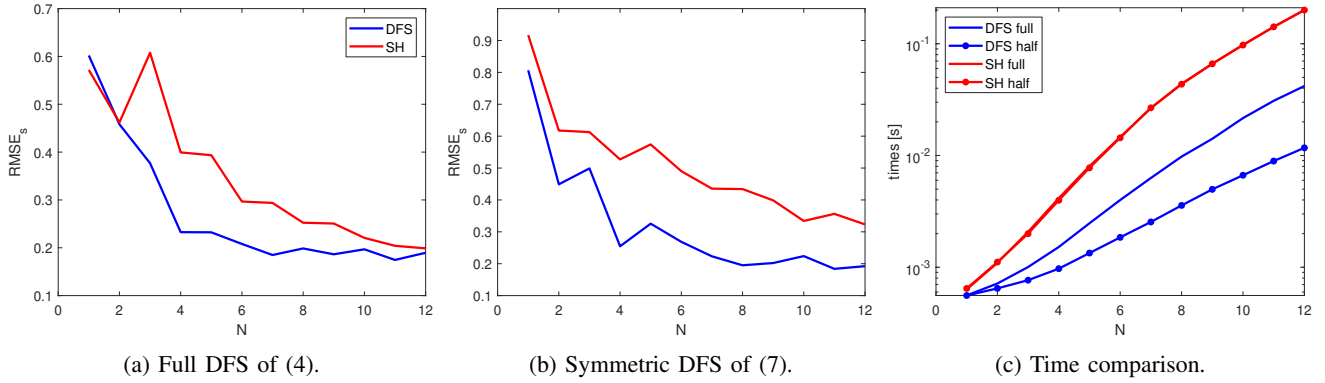


Fig. 3: Monte Carlo simulation of static shape estimation using spherical DFS and spherical harmonics.

A. Static scenario

In the static scenario, shape estimation is performed for different degrees N and performance is compared after convergence. The shape estimation outcome is analyzed using shape root mean squared errors (RMSE) as defined in (19). Thus, angles $\theta_i \in [0, \pi]$ and $\phi_j \in [0, 2\pi]$ are sampled and related radii r_{ij} and \hat{r}_{ij} of the reference and the estimation respectively are calculated. Subsequently, the RMSE

$$\text{RMSE}_s = \sqrt{\frac{\sum_{i=1}^n \sum_{j=1}^m (\hat{r}_{ij} - r_{ij})^2}{nm}} \quad (19)$$

for shape estimation can be calculated. In Fig. 3, RMSE_s for a static scenario with a cuboid shape after a Monte Carlo simulation of 100 runs are shown. In this simulation, a single measurement is drawn, the shape is estimated, and RMSE_s are calculated at the end of the scenario. Time is measured for an update step of a single measurement using MATLAB R2020b on a Intel(R) Xeon(R) X5680 CPU with 3.33 GHz. For a full spherical DFS, measurements are drawn uniformly distributed from the angle intervals $\theta \sim \mathcal{U}(0, \pi)$ and $\phi \sim \mathcal{U}(0, 2\pi)$, thus from the whole surface. For a spherical DFS with a vertical plane of symmetry, measurements are drawn uniformly distributed from the angle intervals $\theta \sim \mathcal{U}(0, \pi)$ and $\phi \sim \mathcal{U}(0, \pi)$, thus from half the surface. The shape is initialized as Gaussian with mean $\underline{p}_k = [1, \underline{0}^T]^T \in \mathbb{R}^{d_p}$ and covariance matrix $\text{diag}(0.3, \dots, 0.3) \in \mathbb{R}^{d_p \times d_p}$, i.e., as uncertain sphere, for all following experiments. Note that the dimension d_p depends on whether a full or a spherical DFS involving a vertical plane of symmetry is used. The measurements are generated normally distributed around the surface point with a variance of $\sigma_z = 0.1$ m in all three dimensions.

In Fig. 3, it can be seen that shape estimation of a cuboid shape performs best for degree $N = 7$ or higher for both types of spherical DFS presented in Sec. II. This is due to the fact that a cuboid shape entails sharp corners while the shape function is discontinuous. Thus, higher degrees of spherical DFS are needed for an adequate shape estimate. In comparison to shape estimation using spherical harmonics [15], spherical DFS tend to be more accurate in shape estimation precision. Specifically, when measurements are only gathered

from half the target's surface, spherical DFS with a vertical plane of symmetry show a clear improvement in shape estimation. This is particularly important as measurements of common range devices such as multilayer LiDAR sensors or depth cameras only gather measurements of the targets side facing the sensor.

Finally, spherical DFS not only tend to be more accurate than spherical harmonics. They are also faster in computation as can be seen in Fig. 3c. This is mainly caused by the need of computation for associated Legendre polynomials when using spherical harmonics. In our implementation, we use an efficient hard coding of associated Legendre polynomials that is still slower than using spherical DFS. In contrast, spherical DFS are faster in computation and easier to implement as the decomposition only consists of sine and cosine functions. In Fig. 3c, computation time comparison of both spherical DFS and spherical harmonics processing measurements distributed on the full surface and half the surface of a cuboid is illustrated. It can be seen that spherical DFS are much faster in computation, especially when using a representation involving a vertical plane of symmetry.

B. Dynamic scenario

Shape estimation is now investigated in a dynamic tracking scenario. In Fig. 4, the shape estimation and tracking outcome is illustrated for a single simulated scenario with a cuboid shape and measurements drawn uniformly distributed from the angle intervals $\theta \sim \mathcal{U}(0, \pi)$ and $\phi \sim \mathcal{U}(0, \pi)$. Thus, a spherical DFS with a vertical plane of symmetry according to (7) is used in the measurement model (15). The degree of the DFS is chosen as $N = 8$. The number of measurements is simulated as Poisson distributed random number with an average of 30 measurements. Measurement noise was chosen as $\sigma_z = 0.1$ m in all three dimensions.

As motion model, a coordinated turn model with polar velocity [28] is applied for tracking and for reference trajectory generation. For evaluating the robustness of the proposed method, the model in [28] is extended by a roll angle and a roll rate, similar to the yaw angle and yaw rate, however uncoupled to position transition. Thus, system state uncertainties are taken as $\sigma_v = 2.2$ m/s for polar velocity, $\sigma_\omega = 1.5$ deg/s for yaw rate and $\sigma_\psi = 1.5$ deg/s for roll rate.

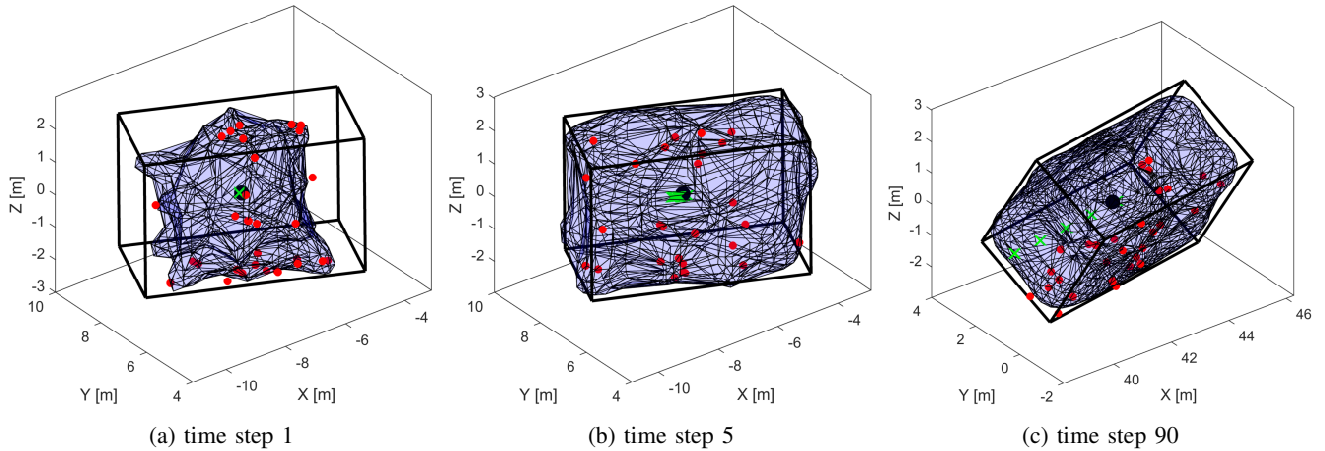


Fig. 4: Simulated tracking scenario of a cuboid at different time steps. The reference cuboid is shown with black lines, reference trajectory with green crosses, estimated center as black dot, measurements as red dots, and estimated shape as light blue surface.

The z -component of position m_k is modeled as being constant over time. As aforementioned, rotation angles can also be stated as quaternions compared to [13] which would lead to modifying the motion model. Shape parameters are chosen to be constant in the dynamic model.

In Fig. 4a, the first time step of the simulated scenario is depicted. It can be seen that the shape function follows the measurements and no larger outgrowths appear. The spherical DFS involving a vertical plane of symmetry is applied as only measurements from the front side are present and shape estimation at the back side still performs well. At time step 5 in Fig. 4b, the shape is already nearly converged. Only a few parts of the shape need some more measurements for a proper shape representation. Finally in Fig. 4c at the end of the scenario, the shape is completely converged. It can be seen that roll and yaw movement can be integrated in 3D shape estimation and tracking using spherical DFS involving a vertical plane of symmetry.

V. COMPARISON OF ORDINARY AND SPHERICAL DFS

In this section, spherical DFS of (2) are compared to ordinary DFS of (1) for EOT in a static scenario. In this simulation, at every time step a single measurement is drawn and the shape of a cuboid is estimated using spherical DFS and ordinary DFS as radial function of measurement equation (15). $RMSE_s$ are calculated for every single measurement update. This simulation is performed with both spherical and ordinary DFS involving a vertical and no plane of symmetry. All presented results of this section show mean values after a Monte Carlo simulation of 100 runs.

In Fig. 5a, convergence rate of spherical and ordinary DFS involving a vertical and no plane of symmetry is illustrated. Markers indicate the value of $RMSE_s$ where differences between single time steps fall below the threshold of 10^{-5} for the first time for different degrees N of spherical and ordinary DFS. Numbers indicate the amount of measurements needed for convergence. In Fig. 5b maximum $RMSE_s$ of a simulation run are depicted for different degrees N . Markers

indicate maximum value while numbers indicate amount of measurements already processed.

In Fig. 5a, it can be seen that spherical DFS converge to lower values of $RMSE_s$, especially involving a vertical plane of symmetry. Additionally, spherical DFS need fewer measurements to converge compared to ordinary DFS. Fig. 5b shows that using ordinary DFS, $RMSE_s$ initially become worse at the beginning and maximum values are very high. Maximum $RMSE_s$ values increase with degree N for both ordinary and spherical DFS, as higher curvatures are possible which can lead to larger deviations compared to the reference shape. In comparison, $RMSE_s$ start to decrease with the first measurement using spherical DFS and maximum values are much lower.

Both effects can be attributed to the pole problem described in Sec. II. Due to the fact that radial functions decomposed using ordinary DFS suffer from ambiguities at the poles, shape estimation needs more measurements to converge compared to spherical DFS. Additionally, larger outgrowths appear at the beginning of shape estimation using ordinary DFS which decrease only after a certain amount of measurements at corresponding locations. Therefore, shape estimation using ordinary DFS gets worse at first while shape estimation using spherical DFS starts converging from the very beginning of the scenario as no ambiguities at the poles have to be resolved.

VI. CONCLUSIONS AND FUTURE WORK

We proposed a novel measurement model for 3D shape estimation using spherical DFS. The shape was estimated using contour measurements assuming a star-convex radial function for shape representation. Our measurement equation can be integrated in nonlinear state estimation techniques like the well-known UKF [27]. To be able to process measurements that stem from the side of the target facing the sensor only, we modified the spherical DFS to involve a vertical plane of symmetry. We investigated our model in comparison to spherical harmonics and ordinary DFS in

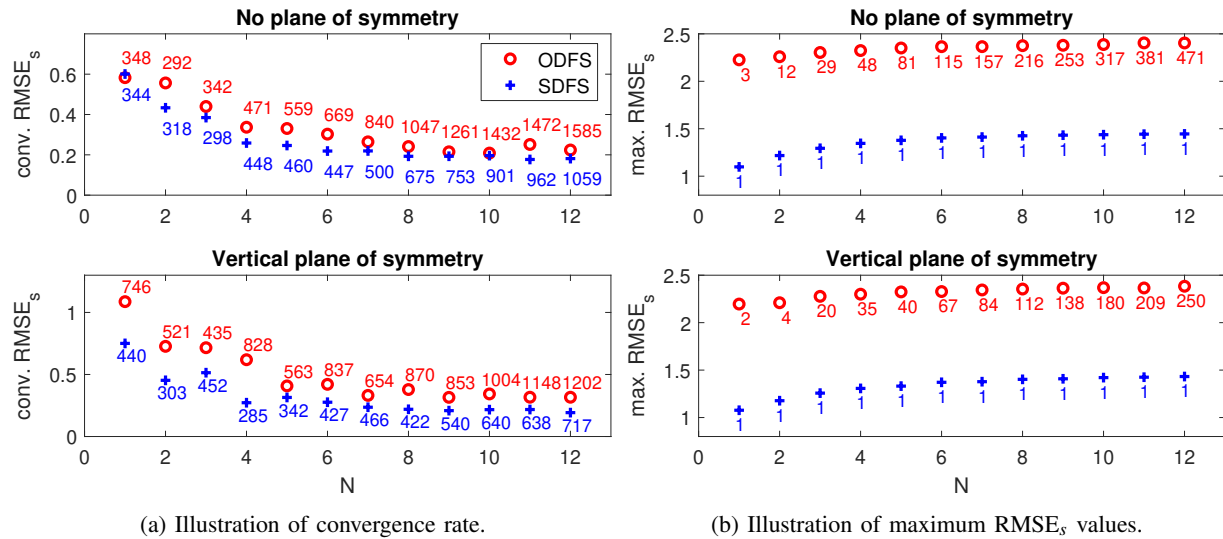


Fig. 5: Results for static comparison of spherical and ordinary DFS in a Monte Carlo simulation of 100 runs.

simulated scenarios. Shape estimation using spherical DFS showed clear advantages in estimation accuracy compared to spherical harmonics and ordinary DFS. In future work we will apply our shape estimation technique to real-world shapes such as cars or ships in simulations and to basic geometric and real-world shapes in real data experiments.

REFERENCES

- [1] K. Granström, M. Baum, and S. Reuter, "Extended object tracking: Introduction, overview, and applications," *Journal of Advances in Information Fusion*, vol. 12, Dec. 2017.
- [2] K. Gilholm and D. Salmond, "Spatial distribution model for tracking extended objects," *IEE Proceedings - Radar, Sonar and Navigation*, vol. 152, pp. 364–371, Nov. 2005.
- [3] M. Feldmann, D. Fränken, and W. Koch, "Tracking of extended objects and group targets using random matrices," *IEEE Transactions on Signal Processing*, vol. 59, no. 4, pp. 1409–1420, 2011.
- [4] M. Baum and U. D. Hanebeck, "Random hypersurface models for extended object tracking," in *IEEE International Symposium on Signal Processing and Information Technology (ISSPIT)*, 2009, pp. 178–183.
- [5] F. Faion, A. Zea, and U. D. Hanebeck, "Reducing bias in Bayesian shape estimation," in *17th International Conference on Information Fusion (FUSION)*, 2014.
- [6] F. Faion, A. Zea, M. Baum, and U. D. Hanebeck, "Partial likelihood for unbiased extended object tracking," in *18th International Conference on Information Fusion (Fusion)*, 2015, pp. 1022–1029.
- [7] P. Broßbeit, M. Rapp, N. Appenrodt, and J. Dickmann, "Probabilistic rectangular-shape estimation for extended object tracking," in *IEEE Intelligent Vehicles Symposium (IV)*, 2016, pp. 279–285.
- [8] K. Granström, C. Lundquist, and U. Orguner, "Tracking rectangular and elliptical extended targets using laser measurements," in *14th International Conference on Information Fusion (FUSION)*, 2011.
- [9] H. Kaulbersch, J. Honer, and M. Baum, "A Cartesian B-spline vehicle model for extended object tracking," in *21st International Conference on Information Fusion (FUSION)*, 2018.
- [10] M. Baum and U. D. Hanebeck, "Shape tracking of extended objects and group targets with star-convex RHMs," in *14th International Conference on Information Fusion (FUSION)*, 2011.
- [11] N. Wahlström and E. Özkan, "Extended target tracking using Gaussian processes," *IEEE Transactions on Signal Processing*, vol. 63, no. 16, pp. 4165–4178, 2015.
- [12] M. Kumru and E. Özkan, "3D extended object tracking using recursive Gaussian processes," in *21st International Conference on Information Fusion (FUSION)*, 2018.
- [13] M. Kumru and E. Ozkan, "Three-dimensional extended object tracking and shape learning using Gaussian processes," *IEEE Transactions on Aerospace and Electronic Systems*, 2021.
- [14] F. Ebert and H. Wuensche, "Dynamic object tracking and 3D surface estimation using Gaussian processes and extended Kalman filter," in *IEEE Intelligent Transportation Systems Conference (ITSC)*, 2019, pp. 1122–1127.
- [15] G. Kurz, F. Faion, F. Pfaff, A. Zea, and U. D. Hanebeck, "Three-dimensional simultaneous shape and pose estimation for extended objects using spherical harmonics," Dec. 2020, preprint arXiv:2012.13580.
- [16] F. Faion, A. Zea, J. Steinbring, M. Baum, and U. D. Hanebeck, "Recursive Bayesian pose and shape estimation of 3D objects using transformed plane curves," in *Sensor Data Fusion: Trends, Solutions, Applications (SDF)*, 2015.
- [17] F. Faion, M. Baum, and U. D. Hanebeck, "Tracking 3D shapes in noisy point clouds with random hypersurface models," in *15th International Conference on Information Fusion (FUSION)*, 2012, pp. 2230–2235.
- [18] A. Zea, F. Faion, and U. D. Hanebeck, "Tracking extended objects using extrusion random hypersurface models," in *Sensor Data Fusion: Trends, Solutions, Applications (SDF)*, 2014.
- [19] H. Cheong, "Double Fourier series on a sphere: Applications to elliptic and vorticity equations," *Journal of Computational Physics*, vol. 157, pp. 327–349, 2000.
- [20] J. P. Boyd, *Chebyshev and Fourier Spectral Methods*, ser. Dover Books on Mathematics. Dover Publications, 2001.
- [21] S. Orszag, "Fourier series on spheres," *Monthly Weather Review*, vol. 102, pp. 56–75, 1974.
- [22] S. Y. K. Yee, "Studies on Fourier series on spheres," *Monthly Weather Review*, vol. 108, pp. 676–678, 1980.
- [23] J. Boyd, "The choice of spectral functions on a sphere for boundary and eigenvalue problems: A comparison of Chebyshev, Fourier and associated Legendre expansions," *Monthly Weather Review*, vol. 106, pp. 1184–1191, 1978.
- [24] H. Cheong, "Application of double Fourier series to the shallow-water equations on a sphere," *Journal of Computational Physics*, vol. 165, pp. 261–287, 2000.
- [25] J. Hanna and J. Rowland, *Fourier Series, Transforms, and Boundary Value Problems: Second Edition*, ser. Dover Books on Mathematics. Dover Publications, 2008.
- [26] G. Tolstov and R. Silverman, *Fourier Series*, ser. Dover Books on Mathematics. Dover Publications, 1976.
- [27] S. J. Julier and J. K. Uhlmann, "Unscented filtering and nonlinear estimation," *Proceedings of the IEEE*, vol. 92, no. 3, pp. 401–422, 2004.
- [28] M. Roth, G. Hendeby, and F. Gustafsson, "EKF/UKF maneuvering target tracking using coordinated turn models with polar/Cartesian velocity," in *17th International Conference on Information Fusion (FUSION)*, 2014.